MASARYKOVA UNIVERZITA
Přírodovědecká fakulta
Ústav teoretické fyziky a astrofyziky

BAKALÁŘSKÁ PRÁCE

Brno 2020 Kateřina Svačinková

MASARYKOVA
UNIVERZITA

Přírodovědecká fakulta
Ústav teoretické fyziky a astrofyziky

Rentgenová spektroskopie polární záře na Jupiteru

Bakalářská práce

Kateřina Svačinková

Vedoucí bakalářské práce:
doc. Mgr. Norbert Werner, Ph.D.

Brno 2020

Bibliografický záznam

Autor: Kateřina Svačinková
Přírodovědecká fakulta, Masarykova univerzita
Ústav teoretické fyziky a astrofyziky

Název práce: Rentgenová spektroskopie polární záře na Jupiteru

Studijní program: Fyzika

Směr: Fyzika

Vedoucí práce: doc. Mgr. Norbert Werner, Ph.D.

Akademický rok: 2019/2020

Počet stran: viii + 38

Klíčová slova: Jupiter, rentgenová spektroskopie, polární záře

Bibliographic record

Author:	Kateřina Svačinková Faculty of Science, Masaryk University Department of Theoretical Physics and Astrophysics
Title of Thesis:	X-ray spectroscopy of Jupiter's auroral emission
Degree Programme:	Physics
Field of study:	Physics
Supervisor:	doc. Mgr. Norbert Werner, Ph.D.
Academic Year:	2019/2020
Number of Pages:	viii + 38
Keywords:	Jupiter, X-ray spectroscopy, aurora

Abstrakt

Jupiter má velmi rozsáhlou magnetosféru. Tato magnetosféra je také zdrojem plazmy, která na Jupiteru pohání silnou polární záři, vyzařující mnoho vlnových délek. Charge exchange je zodpovědný za polární záři v rentgenové oblasti. Vyskytuje se při srážkách urychlených energetických iontů s atomy v atmosféře. Původ těchto urychlených iontů je stále otevřenou otázkou.

Našim cílem je zjistit, odkud pocházejí zrychlené ionty, zda je jejich zdroj v Jupiterově magnetosféře nebo ve slunečním větru. Představujeme spektrální analýzu čtyř spekter Jupiterovy polární záře, získaných pomocí XMM-Newtonu v únoru a březnu 2007. Zjistili jsme, že jedno ze spekter bylo nejlépe popsáno pomocí Iogenního S:O modelu, který předpokládá, že urychlené ionty pocházejí z Jupiterova měsíce Io. Model slunečního větru poskytl lepší fit pro další spektrum. Zbývající dvě spektra byly popsány shodně oběma modely. Brzdné záření (bremsstrahlung) je zodpovědné za spojitou část rentgenové emise polární záře. Charge exchange model s brzdným zářením zlepšil kvalitu fitu v jednom případě.

Zjistili jsme, že jak sluneční vítr tak Iogenní proces by mohli přispívat k emisi CX spojené s rentgenovou polární září na Jupiteru.

Abstract

Jupiter harbours a large magnetosphere. This magnetosphere is also a source of plasma, which powers the prominent multi-wavelength auroral emission that takes place on Jupiter. Charge exchange is responsible for aurorae in the X-ray wavelength. It occurs during the collisions of accelerated energetic ions with atoms in the atmosphere. The origin of these accelerated ions is still an open question.

Our goal is to determine, where the accelerated ions come from, whether their source is in Jupiter's magnetosphere or in the solar wind. We perform a spectral analysis of four Jupiter's auroral spectra, obtained by XMM-Newton in February and March 2007. We find that one of the spectra was best described by the S:O Iogenic model, which assumes that the accelerated ions originate in Jupiter's moon Io. The solar wind model showed the best fit for another spectrum. The remaining two spectra were described well by both models. Bremsstrahlung emission is responsible for the continuum part of the X-ray auroral emission. The charge exchange model with bremsstrahlung emission improved the quality of the fit in one case.

We find that both the Iogenic and solar wind process could possibly contribute to the CX emission associated with the X-ray aurorae of Jupiter.

MUNI
SCI

MASARYKOVA UNIVERZITA
PŘÍRODOVĚDECKÁ FAKULTA
KOTLÁŘSKÁ 2, 611 37 BRNO
IČ: 00216224
DIČ: CZ00216224

ZADÁNÍ BAKALÁŘSKÉ PRÁCE

Akademický rok: 2019/2020

Ústav:	Ústav teoretické fyziky a astrofyziky
Studentka:	Kateřina Svačinková
Program:	Fyzika
Obor:	Fyzika

Ředitel *Ústavu teoretické fyziky a astrofyziky* PřF MU Vám ve smyslu Studijního a zkušebního řádu MU určuje bakalářskou práci s názvem:

Název práce:	Rentgenová spektroskopie polární záře na Jupiteru
Název práce anglicky:	X-ray spectroscopy of Jupiter's auroral emission
Jazyk závěrečné práce:	

Oficiální zadání:

Jupiter produces diverse and dynamic multi-waveband auroral emissions. Radio, infrared, visible, ultraviolet and X-ray auroral emissions have all been observed from the planet. The student will investigate X-ray spectra of Jupiter's aurorae obtained by the EPIC instrument on the XMM-Newton satellite during four observations in February and March 2007. The goal is to determine the emission mechanism and learn about the physical processes behind the production of the variable X-ray emission in the polar regions of Jupiter.

Vedoucí práce:	doc. Mgr. Norbert Werner, Ph.D.
Datum zadání práce:	2. 12. 2019
V Brně dne:	8. 1. 2020

Souhlasím se zadáním (podpis, datum):

....	....	....
Kateřina Svačinková **studentka**	doc. Mgr. Norbert Werner, Ph.D. **vedoucí práce**	prof. Rikard von Unge, Ph.D. **ředitel Ústavu teoretické fyziky a astrofyziky**

Poděkování

Na tomto místě bych chtěla poděkovat svému vedoucímu doc. Mgr. Norbertu Wernerovi, Ph.D. za trpělivost a množství času strávené odborným vedením této práce. Také bych chtěla poděkovat rodině a svým blízkým přátelům za velkou podporu v období studia.

Prohlášení

Prohlašuji, že jsem svoji bakalářskou práci vypracovala samostatně pod vedením vedoucího práce s využitím informačních zdrojů, které jsou v práci citovány.

Brno 17. srpna 2020

Podpis autora

Contents

Introduction

X-rays have become an important source of information about our solar system. Astrophysical X-rays are usually associated with very hot plasmas, an example of this is the hot solar corona. Although the bodies of the solar system, besides the Sun do not contain hot plasmas, they still emit X-rays. Solar system X-rays were discovered in 1950, and they were observed from the Moon in 1962. In 1970 the first X-ray satellite Uhuru was launched. In 1996, the ROSAT satellite discovered radiation from comets, which revealed the important solar wind charge exchange process, occurring throughout our solar system. At the turn of the millennium, the XMM-Newton and Chandra satellites, with their great spatial and spectral resolution provided important information for studying X-rays in the solar system (Bhardwaj et al., 2007).

The fact that Jupiter has a very strong magnetic field was discovered in 1954 using radio observations. Jovian magnetosphere is rotationally based, with large plasma sources in the inner magnetosphere, originating from the Io plasma torus. The first X-rays from Jupiter were discovered in 1979 using the Einstein X-ray Observatory satellite. It was expected that X-rays from Jupiter consist of bremsstrahlung emissions, but its spectrum was more like cometary spectra, from which it can be concluded that Jupiter is dominated by the charge exchange process. Many measurements of Jupiter's X-ray emission were made with XMM-Newton and Chandra providing important insights about the processes in Jupiter's complicated magnetosphere, the analysis of which is key for understanding the X-ray auroral mechanism (Bagenal et al., 2017; Bhardwaj et al., 2007; Branduardi-Raymont et al., 2007).

Chapter 1

Auroral processes on Jupiter

1.1 Key magnetospheric regions of Jupiter

Jupiter's strong magnetic field makes the magnetosphere of Jupiter the largest objects within the heliosphere. The Jovian magnetosphere is subdivided into three parts: the inner magnetosphere, which has a radius smaller then 10 Jupiter radii (R_J), the middle magnetoshpere, located at a distance of 10-40 R_J and the outer magnetosphere with a radius over 40 R_J. Three conditions are required in order to maintain a magnetosphere: a planetary magnetic field that is strong enough to cease the solar wind, to maintain the population of particles in the magnetosphere; a source of plasma, and a source of energy. In the case of Jupiter's and Saturn's magnetospheres, the energy originates from planetary rotation and the plasma is derived from the planet or its satellites. However, the solar driven magnetospheres (e.g. Mercury or Earth) derive their plasma and energies mainly from the solar wind (Khurana et al., 2004).

The Galilean moon Io ($\sim 6\ R_J$) delivers approximately one ton per second of neutral gas to the inner magnetosphere. This neutral gas comes from its SO_2 atmosphere, due to Io's volcanoes and surface sublimation. The neutral gas is then dissociated, ionized and trapped by the magnetic field. As a result the plasma torus with a density $\sim$ 2000 particles/cm^3, is formed in the inner magnetosphere. This plasma torus then tries to co-rotate with Jupiter's $\sim$ 10 hours spin period. The neutral atoms, escaping from Io, move close to Io's orbital speed of 17 km/s. Due to collisions with thermal electrons, oxygen and sulfur ions are ionized, which leads to gain of energy. The ions then move under the influence of an electric field, consequently they develop a gyromotion at a speed of 57 km/s. These highly charged ions then move equally with the surrounding co-rotating plasma at co-rotating speed (Bagenal et al., 2017).

The plasma flow is moving faster than the Keplerian orbital velocities of the Galilean moons. Perturbations around Galilean moons occur as an effect caused by the differences between these velocities. The perturbations than propagate along the magnetic field as Alfvén waves. The moons have also a local interaction with the jovian magnetic field, resulting in auroral footprints (Badman et al., 2015).

1.1.1 Plasma sheet

As mentioned above, a dense plasma torus is formed in the inner magnetosphere, due to escaping particles from the Galilean moons (mainly from Io). The plasma slowly moves outward from Io's orbit. At this distance the plasma β (ratio of particle energy density and magnetic energy density) is < 0.2 and the effects of plasma on magnetic field are minimal. At a distance of about 15-20 R$_J$, the plasma starts to lag the corotation and its speed is slowly decreasing. Plasma β is now grater than unity. Beyond 40 R$_J$, Jupiter's ionosphere is not able to transfer sufficient angular momentum and β is rising to over 100. Radial profile of plasma β is displayed in Figure 1.2. Despite of expectations that plasma should cool during expansion into larger volume, the temperature of plasma particles is rising. The reason for this phenomena remain unknown (Khurana et al., 2004; Bagenal et al., 2017). Radial profile of ion temperature is shown in Figure 1.1.

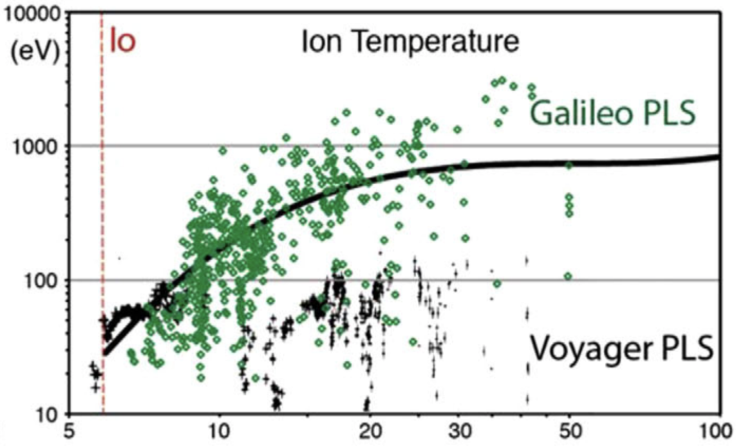

Figure 1.1: Radial profile (the X-axis is displayed in Jupiter radii) of the ion temperature along the equator (Bagenal et al., 2017)

The plasma sheet is located close the dipole magnetic equator, which is the region with the weakest magnetic field. The reason, why the plasma particles are gathering in this region is because of mirror forces of gyrating plasma particles in non-uniform magnetic field (Khurana et al., 2004).

1.1.2 Field-aligned current system

As the plasma moves outward through the magnetosphere and its speed begins to slow down, the pressure of the energetic particle populations inside the magnetosphere dominates over the local magnetic field pressure (i.e. $\beta > 1$), then the particle pressure inflates and stretches out the magnetic field, generating strong currents in the equatorial plasma disk (Bagenal et al., 2017). Thus the magnetic field lines, frozen into the plasma are sub-corotating. These field lines

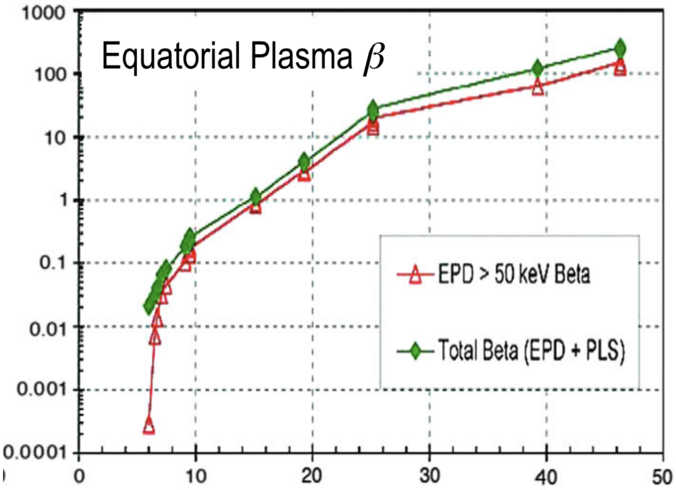

Figure 1.2: Radial profile (the X-axis is displayed in Jupiter radii) of plasma β along the equator. The distribution of plasma is based on Voyager and Galileo data (Bagenal et al., 2017)

have their ends in the ionosphere where collision of energetic ions and neutral atoms can occur. Consequently, the planet supplies angular momentum to the magnetic field, attempting to spin the field and plasma back to co-rotation (Badman et al., 2015).

For maintaining the co-rotation of plasma, strong field-aligned currents are required. This field-aligned current system is direct upward from the ionosphere, radially outward in the equatorial middle magnetoshpere (such as the $\vec{J} \times \vec{B}$ force acts in the direction of planetary rotation), returning downward to the ionosphere at higher latitudes, and closing through an equatorward ionospheric current, as we can see in Figures 1.3 (Cowley and Bunce, 2001; Hill, 2001; Badman et al., 2015).

Figure 1.3 also illustrates the possible configuration of the field-aligned current structure. The equatorially stretched magnetic flux tubes are associated with the strong azimuthal currents that flow in the plasma sheet. Radial currents through the plasma sheet are closed into/out of the ionosphere via field-aligned currents (Bagenal et al., 2017).

There are multiple pairs of downward and upward currents, the exact position of these currents is not known. Based on experience on Earth, the figures of currents system are not precisely accurate. They are likely much more structured and variable than suggested. The analysis of data in the plasma sheet by Mauk and Saur (2007) indicates, that there are multiple pairs of upward and downward currents.

Cravens et al. (2003) suggested two scenarios that could lead to X-ray emission observed from the polar regions. For the first scenario was suggested that highly charged solar wind heavy ions precipitate into the atmosphere and produce X-ray emissions due to solar wind charge exchange (SWCX). For the second

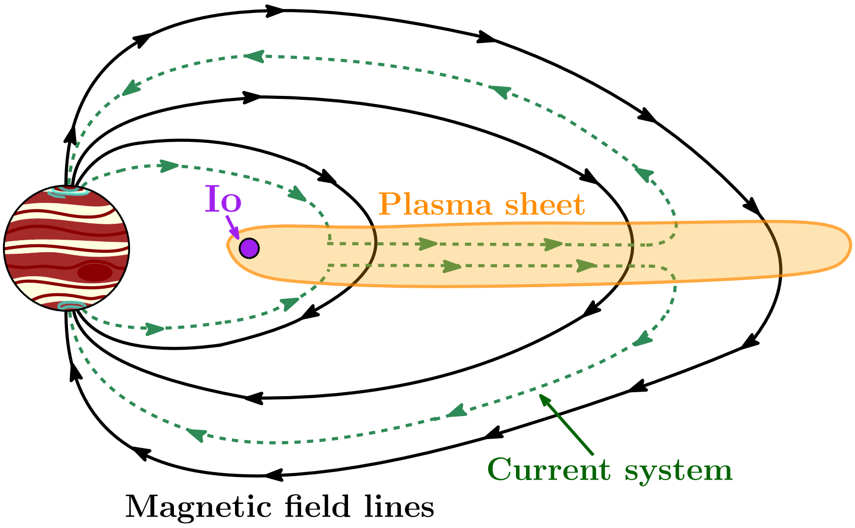

Figure 1.3: An illustration of the field-aligned current system.

scenario, heavy ions (mainly Oxygen and Sulfur), residing in the magnetosphere, precipitate into the atmosphere, where these high charged state ions collide with atmospheric neutrals. They than undergo charge exchange to take an electron from a neutral and emit an X-ray photon. In the first case, the solar wind heavy ions do not have enough energy to produce X-ray emission with a power that was observed. They must therefore undergo additional acceleration by $\sim$ 200 kV field-aligned potential. The heavy ions with magnetospheric origin have even less energy, and they must be accelerated by field-aligned potential of about 8 MV or greater.

1.2 X-ray emission mechanisms

There are several types of X-ray emission observed from inside the Solar system. The X-ray photons can be created by collision of charged particles, like electrons, with neutral atoms and ions. During this collision a fast electron hits an electron from a lower shell of an atom or ion, leaving a hole in this shell. Another electron can collide with this atom and fill the hole. Its energy will then be emitted as recombination radiation. As another option electron from higher shell can fill the hole by descending with simultaneous emission of X-ray photon. This type of emission can make minor contribution to disk emission of outer planets, however, it is dominant for disk emission of Venus and Mars and can also occur when photons are absorbed by the solid surface as it is in the case of the Moon. Another emission mechanism is solar photon scattering from planetary atmospheres. In this process solar photons can be elastically scattered by atoms and molecules inside planetary atmospheres, which act as mirrors. Nonetheless, cross-sections for photon absorption are much higher than those for scattering, hence only a small fraction of incident solar X-ray photons will be reflected from the target atmospheres. Such behavior was observed on Earth, Venus, Mars and in a smaller relative amount in the disks of outer planets. Other ongoing processes are charge exchange and bremsstrahlung continuum emission, which take place in the aurora of Jupiter and will be described in more detail in the following sections (Bhardwaj et al., 2007).

1.3 X-ray auroral spectra

The X-ray spectra of polar regions are well described by a combination of emission lines and bremsstrahlung continuum. Energetic highly charged ions (e.g $O^{7+,8+}$) collide with neutral atoms in Jupiter's atmosphere. During this impact, electrons are exchanged between the neutrals and the charged ions. As a result atmospheric neutrals or molecules are left in an excited state and subsequently decay with the emission of characteristic soft X-ray lines.

This process is commonly observed in our Solar system, the local interstellar medium, supernova remnants, star formatting regions and starburst galaxies. The exospheric X-ray emission of Venus, Mars and Earth are caused by SWCX. In the case of Jupiter's aurorae the origin of the ions is a matter of debate. The ions originate either from the inner magnetosphere (i.e Io's volcanoes) or from the solar wind (Badman et al., 2015).

1.3.1 Emission lines

X-ray line emission detected from Jupiter's aurora, can be well interpreted using the Charge exchange (CX) model. CX processes with astrophysical relevance were firstly discovered in cometary spectra in 1996 during X-ray measurements of the comet Hyakutake by the ROentgen SATellite (ROSAT) observatory (Lisse et al., 1996). Cravens (1997) later suggested that charge transfer between solar wind highly charged ions and neutral gas around the comet is responsible for cometary X-ray emission.

Charge exchange process

Charge exchange is a transfer of one or more electrons between atoms and ions. The most common, however, is the transfer of an electron from a neutral atom to a highly charged ion, where ions act as projectiles with their high speed. In contrast to ions, neutral atoms act as targets and their speed is negligible compared to ions. Still transfer between ions can also occur, but the cross-sections for this process are very small due to Coulombic forces. The charge exchange process appears during collisions and at the time of the impact the electric fields of atom's and ion's nuclei and electrons are superposed. The energy levels of ion and atom overlap at "curve crossings" at certain distances between nuclei, consequently electron can transfer from the target atom to the projectile ion, without any emission of electromagnetic radiation. Because the energy levels can overlap on more then one inter-nuclear distance, electron can transfer to more than one energy level. If the recipient ion is highly charged, the electron will be captured to high-n level, because higher energy levels will overlap with neutral atom's energy levels. This electron will than radiatively decay with emission of X-ray photons, either from undergoing a radiative cascade or by directly decaying to the ground state (Wargelin et al., 2008).

A simple equation can be used to calculate the overall X-ray power density

$$P_x = \alpha n_{sw} n_n u_{sw} \quad (eV cm^{-3} s^{-1}), \tag{1.1}$$

where α is the efficiency factor, which is proportional to the relative abundance of heavy ions in the solar wind and average charge exchange cross section for high charged state ions. n_{sw} is the solar wind density, n_n is the density of target neutral species and u_{sw} is the solar wind speed (Cravens, 2000).

Charge exchange in Astrophysics

Solar wind charge exchange (SWCX), where highly charged Solar wind ions collide with neutral atoms occurring in the Solar system is turning out to be a greatly relevant process in astrophysics. Probably the most explored SWCX is in the case of comets, when this model was discovered and established in the cometary spectra.

A different type of SWCX is when solar wind ions interact with planetary atmospheres. The signs of CX were observed so far on planets Jupiter and Mars mostly with the Chandra X-ray observatory and XMM-Newton (Wargelin et al., 2008).

The X-ray analysis of Mars showed disk emission caused by fluorescent scattering. Other than disk emission there was also found a faint X-ray halo around the disk, generated by SWCX (Gunell et al., 2004).

CX process has been observed in Jupiter's aurorae as well. As discussed in this thesis, it is not clear if this emission is caused by solar wind ions or by ionized atoms from Io's Plasma Torus.

Despite the fact that Venus is located closer to the Sun than Mars and Jupiter, and thus the solar wind density in its vicinity is higher, the X-ray emission from Venus is very weak. On average there is one X-ray photon in $5 \cdot 10^{11}$ photons detected from Venus. The signs of CX processes on Venus were not been detected yet, but they should be present (Dennerl, K. et al., 2002). Dennerl, K. et al. (2002) analysed the X-ray data of Venus and tried to compare the observed spectra with comets. They did not find any similarities, probably due to the small detected count rate.

CX has also been observed in the Earth's exosphere, where X-ray emission showing solar variation was revealed in the background of Earth-orbiting X-ray satellites. The method used for analysing this geocoronal emission was provided by a series of Chandra measurements of the Moon, which blocked the cosmic

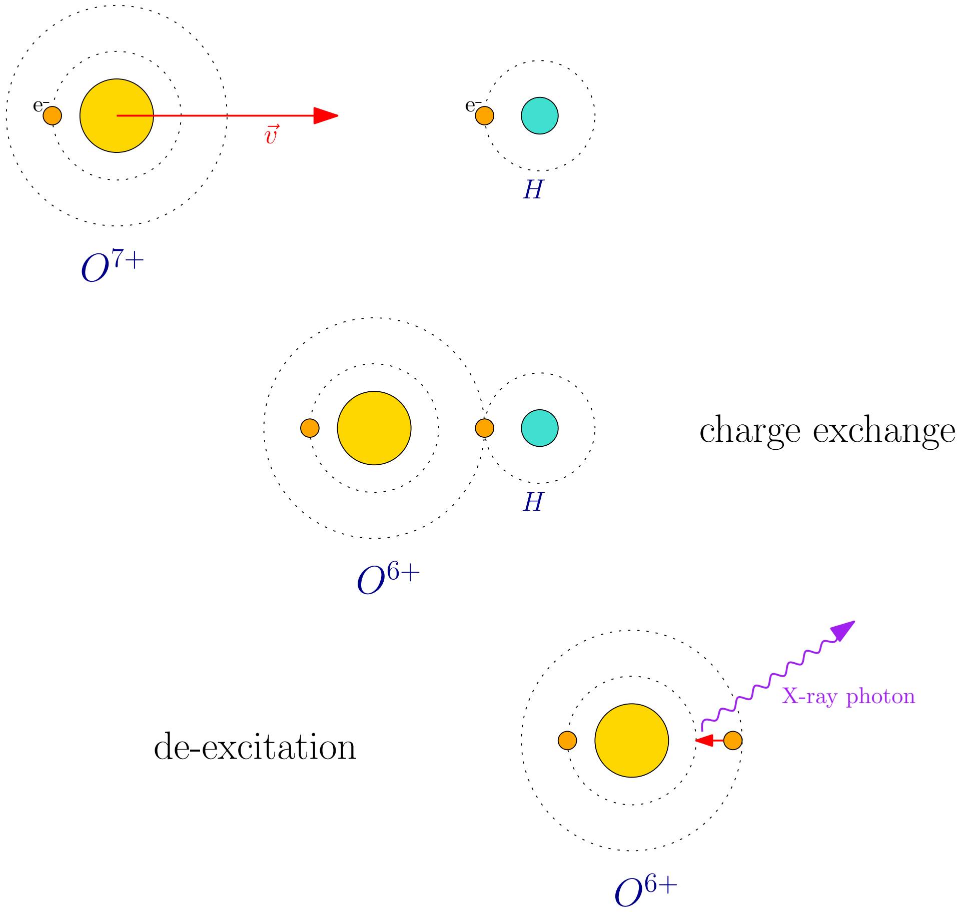

Figure 1.4: An illustration of the charge exchange process.

X-rays. The geocoronal CX process is strongest on the sunward side, where the Earth's magnetosphere is compressed by the solar wind and the density of the neutral population is greater. In contrast, in the dawnward side, the solar wind ions do not reach areas of such high density and they are carried away to the magnetotail region (Wargelin et al., 2008).

The heliosphere contains neutral hydrogen and helium atoms that have entered the Solar system from the interstellar medium. These atoms then undergo charge exchange with solar wind ions and produce X-ray emission. Based on the data of this CX process, the variation of solar wind flux and composition can be determined as well as the distribution of interstellar neutrals in the heliosphere (Cravens, 2000). Wargelin and Drake (2001) showed that similar analysis can be done with nearby dwarf star systems, which would provide information about wind geometry, mass loss rates, ion composition and distribution of neutrals in the interstellar medium. They also suggest usage of

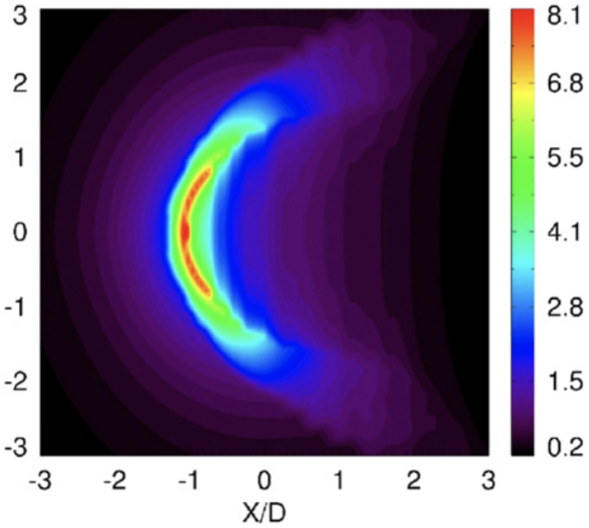

Figure 1.5: Simulation of the X-ray geocoronal emission of the Earth, observed from 50 R_E. The brightness scale units are keV/cm^2/s/sr. X is coordinate in image plane in D units (distance to the magnetopause). From Bhardwaj et al. (2007).

CX emission in the study of astrospheres of nearby stars.

Although SWCX is well established, there are other CX processes. For example, the question is whether X-ray emission from the Galactic ridge and Galactic center is to some extent made up of CX, where the neutrals would react with cosmic rays. In the matter of Galactic ridge this statement is inconclusive, on the other hand in the case of Galactic center there is solid evidence of CX contribution. The analysis of the 511-keV annihilation line revealed that almost all of the emission came from electron-positron annihilation and almost half of these positrons participate in CX with neutral atoms. However, the energies of created photons are more in the gamma-ray part of the spectra. CX can also have influence on photoionized plasma, when photoionization corss-section for hydrogen atoms is for higher energies smaller than CX cross-section, so for highly charged ions CX dominates. For non-equilibrium plasmas such as supernova remnants and evaporating clouds CX can occur, mainly with hot shocked plasma and cool dense clouds within the supernova remnant. No such emission was yet detected, probably because it is difficult to detect CX features (Wargelin et al., 2008).

1.3.2 X-ray continuum emission

The continuum part of the X-ray spectrum of Jupiter's aurora can be well described by bremsstrahlung emission. This radiation is a consequence of classical electrodynamics. The electrons are slowed down by Coloumbic forces between the electrons and nuclei of atoms. According to classical electrodynamics these electrons have to emit continuous electromagnetic radiation. The Bremsstrahlung process is an important part of hard X-ray emission in Earth's and Jupiter's aurora, where fast electrons precipitate into the planet's atmosphere. The total power of continuous emission is much less than the power of line emission (Bhardwaj et al., 2007).

1.4 Auroral morphology

Jupiter's aurorae in the UV wave band exhibit several features. There are different types of auroral emission, implying various processes responsible for it. The composition of the auroral oval consists of three main parts, which are the main oval, the magnetic moon footprints and the polar region. The morphology of the northern aurora is shown in Figure 1.6.

The main emission is aligned with the magnetic pole and co-rotates with the planet, in contrast to the Earth where the aurora stays at the same orientation. Solar wind variations have almost no influence on the main aurora. It has more of a kidney shape than oval, which could be due to a weak magnetic field or anomaly in the magnetic field. The location of main auroral emission was traced

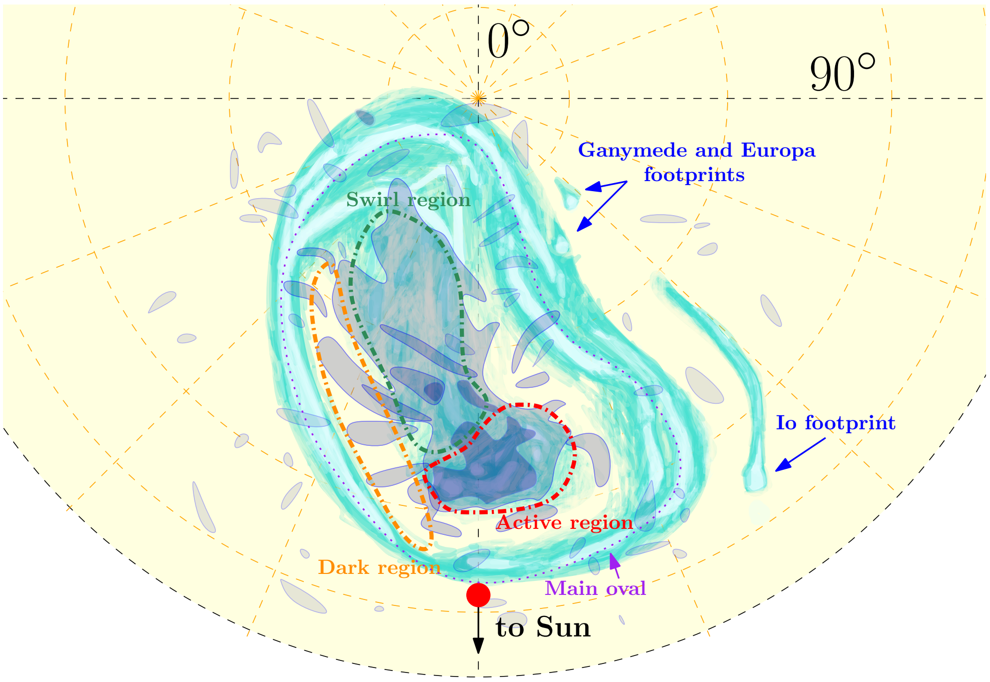

Figure 1.6: Jupiter's UV and X-ray auroral morphology in the northern hemisphere. Light blue color indicates UV light, dark blue shows X-ray emission. Based on Hubble Space Telescope and Chandra X-ray Observatory observations.

to distance of 20-30 R_J, where plasma is constantly produced and therefore the main emission is relatively stable and it does not vary with changes of solar wind conditions (Bagenal et al., 2017; Clarke, 2012; Clarke et al., 2007).

The distance of the main oval's origin was traced based on the known positions of the satellites, which leave magnetic footprints in the auroral emission. The brightest footprint belongs to the moon Io. Its footprint was studied and it shows brightening when Io is centred in Io's plasma torus. Study of Io's footprint can provide an inside look to the electrodynamic interaction near the satellite (Clarke, 2012).

The polar region can be further divided into active, swirl and dark region. Bright flares occur in the active area that brighten in time scale of 10-100 seconds and than fade away. These flares are accompanied by strong X-ray emissions. Inside the swirl region is variable emission with slow flows. It is complicated to map the origin of the polar emission, which can lead to the outer magnetosphere, to the dayside magnetopause or to the magnetotail area (Bagenal et al., 2017; Clarke, 2012).

In Figure 1.6, we display the UV and X-ray auroral morphology. The X-ray morphology differs from the UV band. The strongest X-ray emission is located in the active area inside the polar region as indicated by the dark blue color spot and it extends to other areas with lower intensity (Clarke et al., 2007).

Chapter 2

Data analysis

2.1 XMM-Newton

The X-ray Multi Mirror mission, XMM-Newton, was launched on December 10, 1999. It is an ESA Horizon 2000 programme project. On the 10 m long spacecraft Focal Plane Assembly are placed two Reflection Grating Spectrometer (RGS) read out cameras, the European Photon Imaging Camera (EPIC) pn and two EPIC Metal Oxide Semi-conductor (MOS) imaging detectors. Each of these instruments is equipped with charge-coupled-device (CCD) detectors. The Service module then contains the spacecraft sub-systems, the Optical Monitor instrument, star trackers and three X-ray Mirror Modules. There are three telescopes on board of XMM-Newton, each arrayed with 58 Wolter I mirrors. Two of the telescopes are supplied with the RGS and these also contain the EPIC MOS cameras. The third telescope uses pn CCDs. The comparison of pn CCDs and MOS CCDs is shown in Figure 2.1 (Jansen et al., 2001).

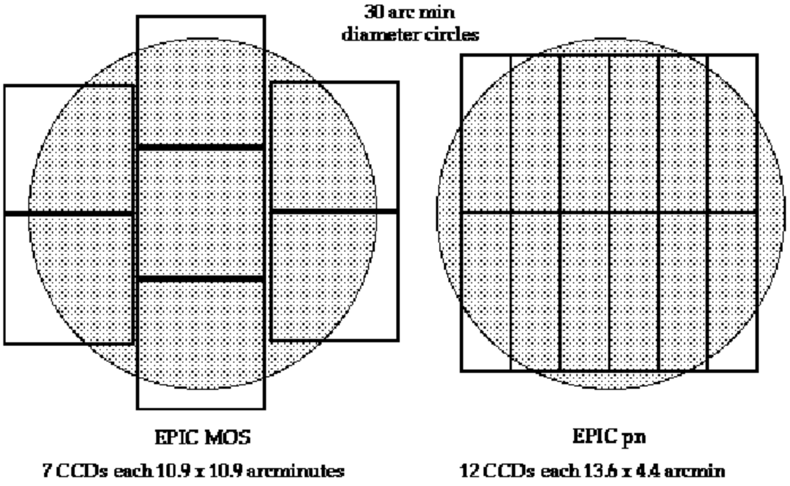

Figure 2.1: Comparison of two types of EPIC instruments on board of XMM-Newton. The light grey circles are 30′ diameter area. From XMM-Newton Users Handbook.

2.1.1 EPIC-pn

In an EPIC-pn instrument, pn-CCD camera serve as X-ray imaging spectrometer.

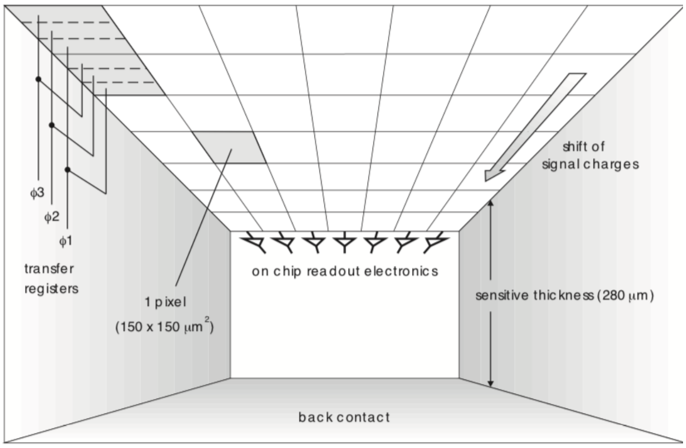

Figure 2.2: Inside view of pn-CCD (Strüder et al., 2001).

A scheme of a pn-CCD is shown in Figure 2.2. As X-rays interact with the chips inside the pn-CCD device, silicon atoms respond to X-rays by generating free electrons and holes. The average energy required to form an electron-hole pair is 3.7 eV at -90° C. Electrons and holes are then separated by strong electric fields, electrons are transferred to a potential minimum and stored under transfer registers, while positively charged holes are moved and absorbed on the back side of the instrument. Each CCD is equipped with a readout amplifier to which the electrons are then relocated, conserving charge distribution patterns from the ionization process. The EPIC-pn instrument contains 12 individually operated 3x1 cm^2 pn-CCDs. The device was adjust for X-ray imaging and spectroscopic mode operating simultaneously by assuming only one X-ray photon will hit the detector without overlap with another photon. To achieve this, the local photon flux should be less than 1/40 events per pixel and integration time. The photon flux can be increased by increasing the area, which will lead to shortened integration time of the CCD camera (Strüder et al., 2001).

2.1.2 EPIC-MOS

Two of three telescopes are equipped with a EPIC-MOS camera. The MOS camera has the same forward section as the PN camera, which contains a filter wheel, a door, a calibration source, radiation shielding, the spacecraft focal plane bulkhead and the internal bulkhead. The difference between the two cameras is mainly in the section containing the CCDs. The two MOS cameras are arranged symmetrically, near the spacecraft sun-shield, and are supplied with long radiators, in contrast to pn cameras. There are 7 CCDs in a MOS camera, one central CCD and 6 outer CCDs. There are two read out nodes on every CCD, which receive the charge generated by X-rays, transferred by pulses.

The EMCR, the control and recognition unit, then converts read outs from each CCD to create an X-ray photon event list. The X-ray spectrum and photon flux is then determined based on the charge measured during an individual photon event obtained from EMCR, the redistribution matrix of the CCD and its quantum efficiency (Turner, L. et al., 2001).

2.1.3 RGS

Two identical RGSs are located behind mirror assemblies. The RGSs are equipped with an array of reflection gratings, placed in the converging beam of the telescope. The grating stack contains 182 aligned reflection gratings, each grating measures about 10 by 20 cm, these gratings must be really flat in order to maintain good resolution and also the grating substrate should be very thin. The grating stack processes about half of the light received by the telescope. The rest of the light passes through and is processed by the EPIC instrument in the telescope's focal plane. The gratings are located in rotating Rowland circle, where the CCDs are also placed. The width of the CCDs is important in order to determine the field of view and the spatial resolution is mostly influenced by the imaging properties of the mirror (in cross dispersion direction). The position of the X-ray photons on the detector gives important information through the dispersion equation

$$m\lambda = d(cos\beta - cos\alpha) \tag{2.1}$$

where m is the spectral order, d is the groove spacing and α and β are the angles of the incident and dispersed photons, respectively (den Herder et al., 2001).

2.2 Spectral analysis

For spectral analysis, we used the SPEX (SPEctral X-ray and UV modeling and analysis) software package. This package was developed for computation and modeling of X-ray and EUV spectra (Kaastra et al., 1996). SPEX provides multiple Spectral models, in order to calculate the best fit for given spectra. In analysing our data we used several of these components.

Jupiter's auroral spectrum is dominated by characteristic emission lines, which occur due to charge exchange processes between highly charged ions and neutral atoms from Jupiter's atmosphere, thus for determining these processes *CX* model was used. This model calculates the spectrum emitted from hot plasma when it recombines with cold neutral materials. *CX* model will be described in more detail in section 2.3. The oxygen was set as reference atom and all other element abundances were set as zero, except the abundances for fitting purposes. Ionization temperature t and normalization $norm$ were set as free and their values were determined by spectral fitting.

An additional component of Jupiter's auroral spectrum is the bremsstrahlung continuum emission, produced by the deceleration of free charged particles. To

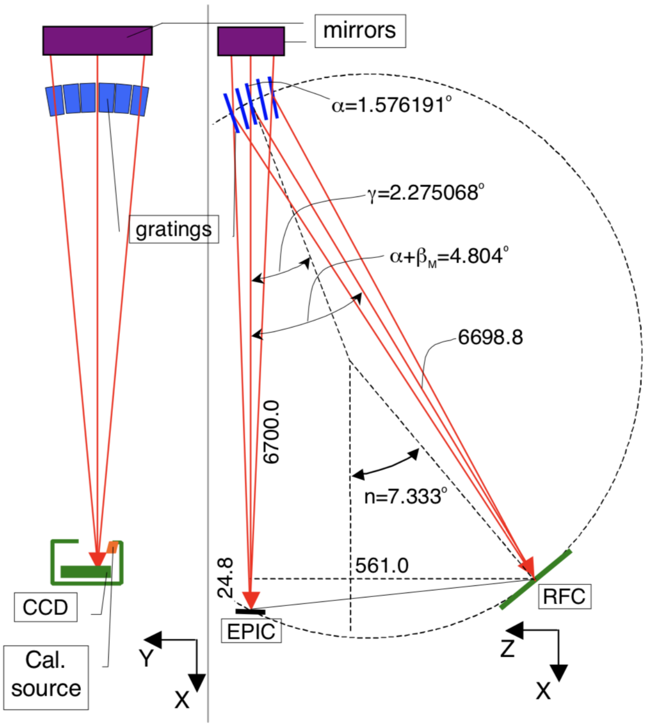

Figure 2.3: Optical design of the RGS (not to scale). Red arrows represent the X-rays. Numerical values for the key distances and angles are written in the image (linear distances in mm, angles in degrees)(den Herder et al., 2001).

include this process the *Cie* model was used. This model calculates the spectrum of plasma in collisional ionisation equilibrium. We set the line emission in the *Cie* model to zero. The temperature parameter t and normalization parameter $norm$ were set as free.

2.3 Fitting Jupiter's spectra with the atomic charge exchange model

The model for astrophysical charge exchange in SPEX, used in this thesis, was created by Gu et al. (2016). This model reproduces the observed spectrum of the comet C/2000 WM1, which is entirely produced by the solar wind charge exchange process. The code is calculated based on three assumptions: firstly, single-electron capture (SEC) in ion-neutral collisions is assumed. The reason for that is that data for SEC are more complete than those for multi-electron capture (MEC), despite the fact that MEC could be important for some environments (such as comets). The second assumption is that CX with atomic hydrogen is representative of the real case in terms of cross-section dependency on ion velocity and state of the captured electron. As third assumption radiative processes as collisional excitation and radiative recombination are neglected to prevent CX transition from being overpowered in emission.

The method used for determining the code to calculate CX line emission is based on finding the ion state distribution after electron capture and than analysing possible radiative decay pathways to the ground state. To obtain the total cross-section as a function of collisional velocity v, they pointed out the usual cross section linear dependency on ion charge q. The following equation is a scaling law used to combine q- and v- dependence

$$\sigma = a_1 q E_s^{a_2} \ln\left(\frac{a_3}{E_s} + a_4\right)\left(1 + \frac{E_s}{a_5}\right)^{a_6} \tag{2.2}$$

where E_s is the scaled collision energy in eV/amu and a_1 to a_6 are the average best-fit values. The total cross section dependency on collision velocity is displayed in Figure 2.4.

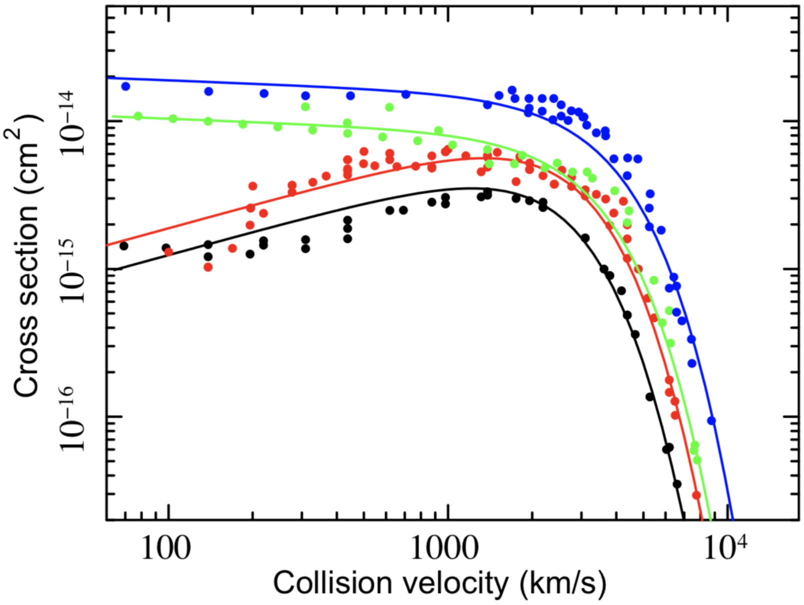

Figure 2.4: Total cross sections, as functions of collision velocity, for B^{5+} (black), O^{8+} (red), Ne^{10+} (green), and Ar^{18+} (blue) interacting with a hydrogen atom. The data points are actual values from previous calculations, and solid lines are the scaling law according to equation 2.1 (Gu et al., 2016).

For n-shell populations, the maximum probability of CX occurs, when two energy states, before and after transition, are most close to each other. The potential energy is relevant for the interaction and the peak level is established by the combination of target atom's and projectile ion's potential ($v \ll v_0$, where v_0 is the orbital velocity of an electron in an atom). The principal quantum number n_p of the most populated energy level is

$$n_p = \sqrt{\frac{I_H}{2I_t}} q \left(1 + \frac{q-1}{\sqrt{2q}}\right)^{-0.5} \tag{2.3}$$

where I_t is the ionization potential of the target atom and I_H is the ionization potential of a hydrogen atom. For l-shell population, the distribution function is approximate as certain weighting function, the preferred weighting function dependent on v and n. To reach complete cascade calculations they obtained energies and transition probabilities up to n=16, which exceeds the maximum capture state for all ions used in the code.

For more detail, including the high speed collision model and l-shell weighting functions see Gu et al. (2016).

2.4 Observations

Jupiter is the largest planet in our Solar system and thus an important object of interest. An example of one of today's unsolved problems in planetary physics is our understanding of its large rotation-driven magnetosphere. For ground-based and Earth-orbit observations a key region for studying Jupiter is its aurora, which can tell us a lot about its magnetospheric properties, precipitating ion population, solar wind influence, etc.. Multi-waveband measurements of Jupiter and its aurora were taken in the past and these observations were studied to determine the properties of Jupiter's behaviour. An examples of some of these observations are shown in figures bellow.

Figure 2.5 shows X-ray images taken by the Chandra X-ray Observatory. The first image shows an X-ray view of Jupiter near the time of observations studied in this thesis (left). At this time Jupiter's distance from the Sun was 5.28 AU, for comparison the picture on the right displays an observation during the solar maximum. The picture taken during the solar maximum is much brighter with strong northern and southern aurora and clear equatorial emission, indicating a strong solar wind influence on the equatorial emission. In Figure 2.6, we show visible and UV images of Jupiter. The picture on the left shows Jupiter's aurora in the UV waveband, projected on a visible image. The picture on the right shows the UV aurora projection. Both images were taken by the Hubble Space Telescope. Figure 2.7 shows an infrared image of Jupiter from the Gemini Observatory. A radio image from the Australia Telescope Array measurements is shown in the picture on the right.

In 2007 February to March, several observations of Jupiter were taken with XMM-Newton, Chandra, Nançay Decameter Array, WIND spacecraft, Hubble Space Telescope and the New Horizons spacecraft. The goal of these long-term observations was to obtain a multi-waveband image of Jupiter's auroral and equatorial emission. In this thesis we work with X-ray auroral spectra taken by XMM-Newton, during the observations listed in Table 2.1.

The 2007 campaign lasted from 8th February to 9th March with several visible, UV, X-ray and radio measurements. This campaign is described and

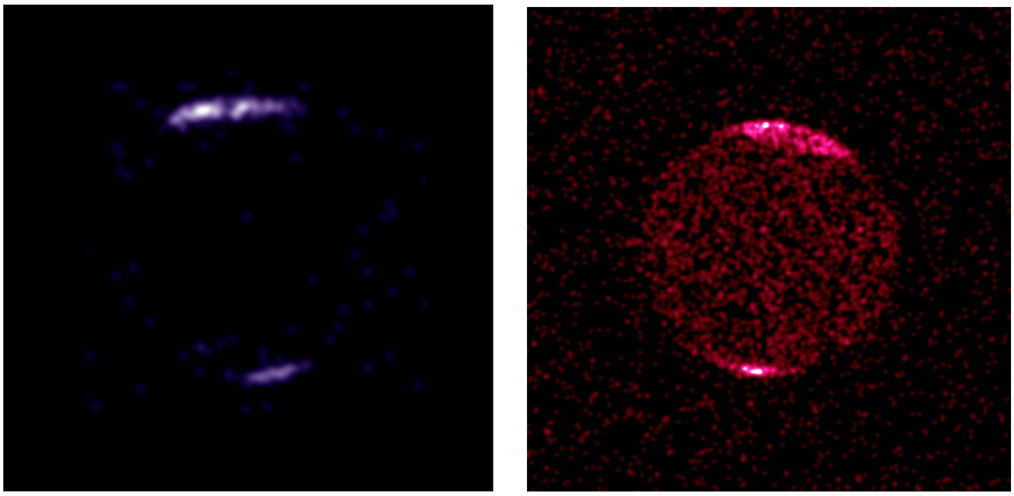

(a) (b)

Figure 2.5: X-ray image of Jupiter taken by Chandra X-ray observatory, (a) shows a co-added image taken during solar minimum, on February 8, 10, and 24 in 2007, (b) an X-ray image of Jupiter taken during the solar maximum on December 18, 2000.

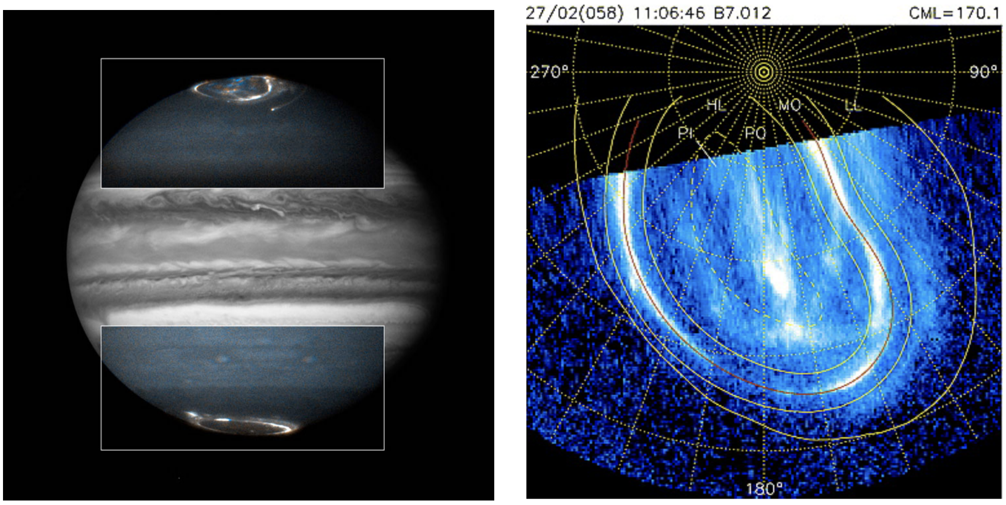

(a) (b)

Figure 2.6: (a) A UV observation of Jupiter with the Hubble space telescope, projected on a visible band image taken on February 17-21th 2007. (b) A UV aurora observed on 27th February 2007, which represents a typical UV auroral projection (Nichols et al., 2009).

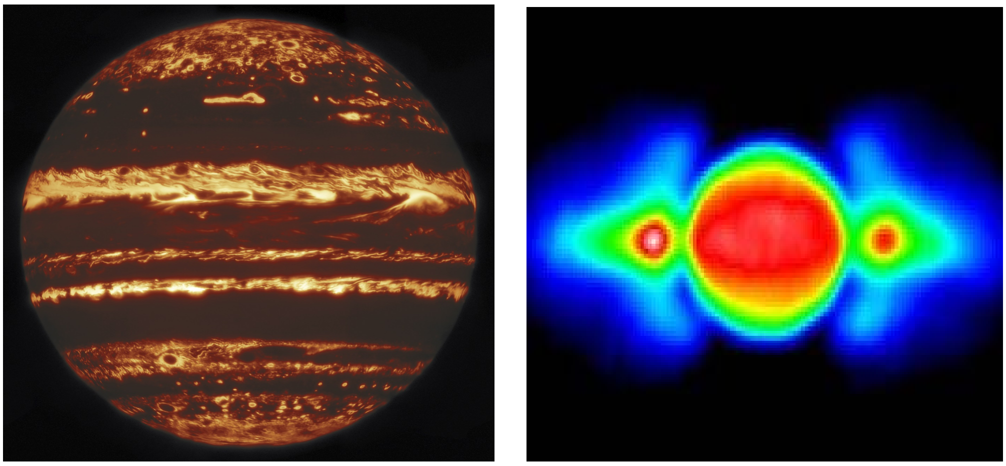

(a) (b)

Figure 2.7: Infrared and radio images of Jupiter. Image shown in (a) is a compiled infrared image of Jupiter (4.7 μm) taken by the international Gemini Observatory on 29th May 2019, (b) shows a radio image from Australia Telescope Compact Array observed between 12 and 26 July 1995.

Date	ID	Time	DOY	CML(°)
24-25 Feb	0413780101	20:14 - 03:02	55-56	47 - 294
3 Mar	0413780201	07:17 - 14:42	62	271 - 180
7 Mar	0413780301	12:52 - 20:21	66	356 - 267
8 - 9 Mar	0413780401	19:50 - 02:20	67-68	39 - 275

Table 2.1: Table of Jupiter's observation's Date, ID, Time, DOY (Day of the year) and CML (Central Meridian Longitude) from XMM-Newton observations in 2007

studied, including UV and radio analysis, in more detail in Dunn et al. (2020a) and Dunn et al. (2020b).

Chapter 3

Results

3.1 Identifying the Precipitating Ion Population

The auroral X-ray emission contributing in the 0.35 - 1 keV energy band was fitted by using SPEX software package. Spectra in Jupiter's polar region show several significant features in the displayed range. Very bright emission between 0.5 - 0.9 keV occurs during all the observations, emitted most likely by oxygen ion CX lines (i.e. OVII and OVIII lines). In the 0.35 - 0.5 keV energy range, we observe an emission feature presumably originating from different charge states of sulfur or carbon ions. Determining whether the emission lines in the 0.35 - 0.5 keV energy band originate from sulfur or carbon ion population is crucial for establishing the origin of the plasma, causing Jupiter's X-ray auroral emission.

We obtained four spectra determined from observations in Table 2.1. These spectra differ from each other, with the spectrum taken on 7th March as the dimmest with the lowest photon flux identified, despite the longest observational time and great auroral visibility at the time. Conversely, the 8-9th March spectrum is the brightest with the largest photon flux. All the photon flux data can be seen in Tables 3.2 and 3.3.

A Gaussian line model was used to determine the observed line energies. The results are shown in Table 3.1. All the spectra show a clear peak at ~ 0.57 keV, corresponding to the oxygen OVII emission line. The peak at ~ 0.70 keV could be caused by a transition of the OVIII ion. The weak ~ 0.89 keV line seen in all the spectra, originates either from solar wind neon ion, suggesting a solar wind impact or from a OVIII transition that could still take place at this energy value. Spectra measured at 3rd March and 8-9th March have a characteristic sulfur/carbon ~ 0.40 keV line. Oxygen lines from 0.35 - 0.5 keV interval could be presumably explained by potential accelerated solar wind ions. An alternative explanation is oxygen ions leaking from Io. Thus determining the ions responsible for the emission is very important for studying the physical processes behind auroral emission.

In the following subsections, we focus first on pure oxygen:sulfur abundance, assuming a magnetospheric origin for the precipitating ions, and subsequently a Solar wind model is used. From this, a line spectrum is calculated and the quality of its fit to the data is determined. We then contrast each model with

Energy(eV)	Identified Ion line	Energy(eV)	Identified Ion line
28-29th Feburary		3rd March	
$580^{+1.1}_{-0.4}$	OVII/OVIII	$590^{+4}_{-0.01}$	OVII/OVIII
$720^{+0.01}_{-250}$	OVIII	$720^{+0.01}_{-200}$	OVIII
$880^{+0.02}_{-560}$	OVIII/NeX	$890^{+0.2}_{-570}$	OVIII/NeX
7th March		8-9th March	
$570^{+4}_{-0.5}$	OVII/OVIII	$580^{+3}_{-0.2}$	OVII/OVIII
$720^{+0.2}_{-470}$	OVIII	$680^{+0.2}_{-160}$	OVIII
		$860^{+0.2}_{-480}$	OVIII/NeX

Table 3.1: Identification of ion lines and their determined energies.

gained ionization temperature, specific element ratio and photon flux of each spectra. All the results are provided with a 1σ error value evaluated by using Poisson statistic. The C-statistic was used to determine the goodness of the fits. In order to process the spectral results Python was applied with special libraries Numpy, Scipy and Matplotlib.

3.1.1 X-ray trends with sulfur:oxygen abundance

If indeed sulphur ions are responsible for the CX process in the energy range of 0.35 - 0.5 keV, then the particles responsible for X-ray line emission originate inside the Io plasma torus.

We set all the element abundances to near zero aside from the sulfur abundance that is a free parameter and oxygen which is the reference element in our model. Several possible combinations of different abundance values and ionization temperatures were tested until the best fit was determined. The best fit parameters are listed in Table 3.2.

In applying Iogenic (S+O) model, the S:O ratio required increasing by up to factor 2. This was probably due to the fact that a single charge exchange (SCX) model was used. This model takes each transit as one line in spectrum and because in the range 0.35 - 0.5 keV a large number of sulfur lines can be present, from S^{6+} to S^{13+} lines in contrast with O^{5+} to O^{7+} oxygen lines in 0.5 - 0.9 keV interval. With the fact that a single ion can descend from S^{13+} through S^{12+}, S^{11+}, S^{10+}, S^{9+}, S^{8+} and S^{7+} on path to S^{6+} means that less sulfur ions are actually needed to produce the observed X-ray emission, as was mentioned in Dunn et al. (2020a).

Date	kT (keV)	Photon Flux (ph/m^2/s)	S:O
24-25 Feb	$0.19^{+0.018}_{-0.011}$	$0.43^{+0.06}_{-0.06}$	$1.06^{+0.25}_{-0.32}$
3 Mar	$0.20^{+0.014}_{-0.013}$	$0.36^{+0.05}_{-0.05}$	$0.86^{+0.22}_{-0.16}$
7 Mar	$0.18^{+0.014}_{-0.013}$	$0.19^{+0.08}_{-0.08}$	$1.11^{+0.64}_{-0.42}$
8 - 9 Mar	$0.19^{+0.006}_{-0.005}$	$0.99^{+0.14}_{-0.14}$	$1.30^{+0.17}_{-0.16}$

Table 3.2: Best fit parameters for Iogenic (S+O) charge exchange model.

3.1.2 X-ray trends with solar wind ion abundance

In order to model a possible solar wind origin for the observed X-ray spectra, we use the solar wind abundances from (von Steiger et al., 2000) summarized in Table 3.3. The ionization temperature and normalization were set as free parameters in our model. Table 3.4 shows the best fit ionization temperatures and photon fluxes.

Element	Abundance
He	95.9 ± 35.1
C	0.67 ± 0.071
N	0.069 ± 0.038
O	1 ± 0
Ne	0.091 ± 0.025
Mg	0.147 ± 0.045
Si	0.167 ± 0.047
S	0.049 ± 0.016
Fe	0.120 ± 0.039

Table 3.3: Solar wind abundances ratios relative to oxygen obtained with Ulysses/SWICS during the four $\sim$ 300-day periods from (von Steiger et al., 2000), abundances are displayed with their 1σ value

Date	kT (keV)	Photon Flux (ph/cm^2/s)
24-25 Feb	$0.18^{+0.006}_{-0.006}$	$0.35^{+0.03}_{-0.03}$
3 Mar	$0.20^{+0.005}_{-0.005}$	$0.23^{+0.05}_{-0.05}$
7 Mar	$0.18^{+0.009}_{-0.008}$	$0.15^{+0.02}_{-0.02}$
8 - 9 Mar	$0.19^{+0.004}_{-0.003}$	$0.66^{+0.04}_{-0.04}$

Table 3.4: Best fit parameters for Solar wind charge exchange model.

3.1.3 Results

The observed Jupiter's auroral spectra and their best-fit models are shown in Figure 3.1. The Iogenic CX model provided better fit for spectra obtained on 24-25th February and 3rd March. Spectra taken on 7th March and 8-9th March were better fitted by the solar wind model.

As we can see, some of the spectra show a weak feature at ~ 0.49 keV, that could also indicate emission lines caused by solar wind CX. However, after fitting a Gaussian line, we found that this feature is not significant.

Date	χ^2/dof	
	S:O	SW
24-25th Feb	0.86	1.70
3rd Mar	1.88	1.91
7th Mar	2.73	2.71
8-9th Mar	1.87	1.55

Table 3.5: χ^2/dof values of best fits determined.

Bremsstrahlung continuum emission

The hard X-ray emission present in Jupiter's auroral spectra shows no line features and is caused by bremsstrahlung continuum. Unfortunately, the observed count rate above 1 keV was very small and it was very hard to distinguish the source emission from instrumental noise.

Including the Bremsstrahlung continuum emission provided a better fit just for the spectrum observed on 24-25th February.

3.2 Connection between Jupiter's aurora and the solar wind

During the time of our observations the New Horizons spacecraft was approaching Jupiter on its way to Pluto, measuring the Solar wind conditions with the Solar Wind Around Pluto (SWAP) instrument. All observations took place at the time of extended solar minimum. During 24-25th February, a maximum of solar wind driven compression occurred with the magnetopause compressed to 50 R_J. This observation happened during the time of the second day of compression from co-rotating interaction region (CIR). CIR appears when the fast solar wind is slowed down at a shock due to the impact with the slow solar wind. At this point the solar wind density increases. When this shock arrives at Jupiter it causes a magnetospheric compression. Rarefaction or arrival of CIR appeared at the time of the 3rd March observation. The 7th March observation occurred during the magnetospheric recovery, when the magnetopause started to expand

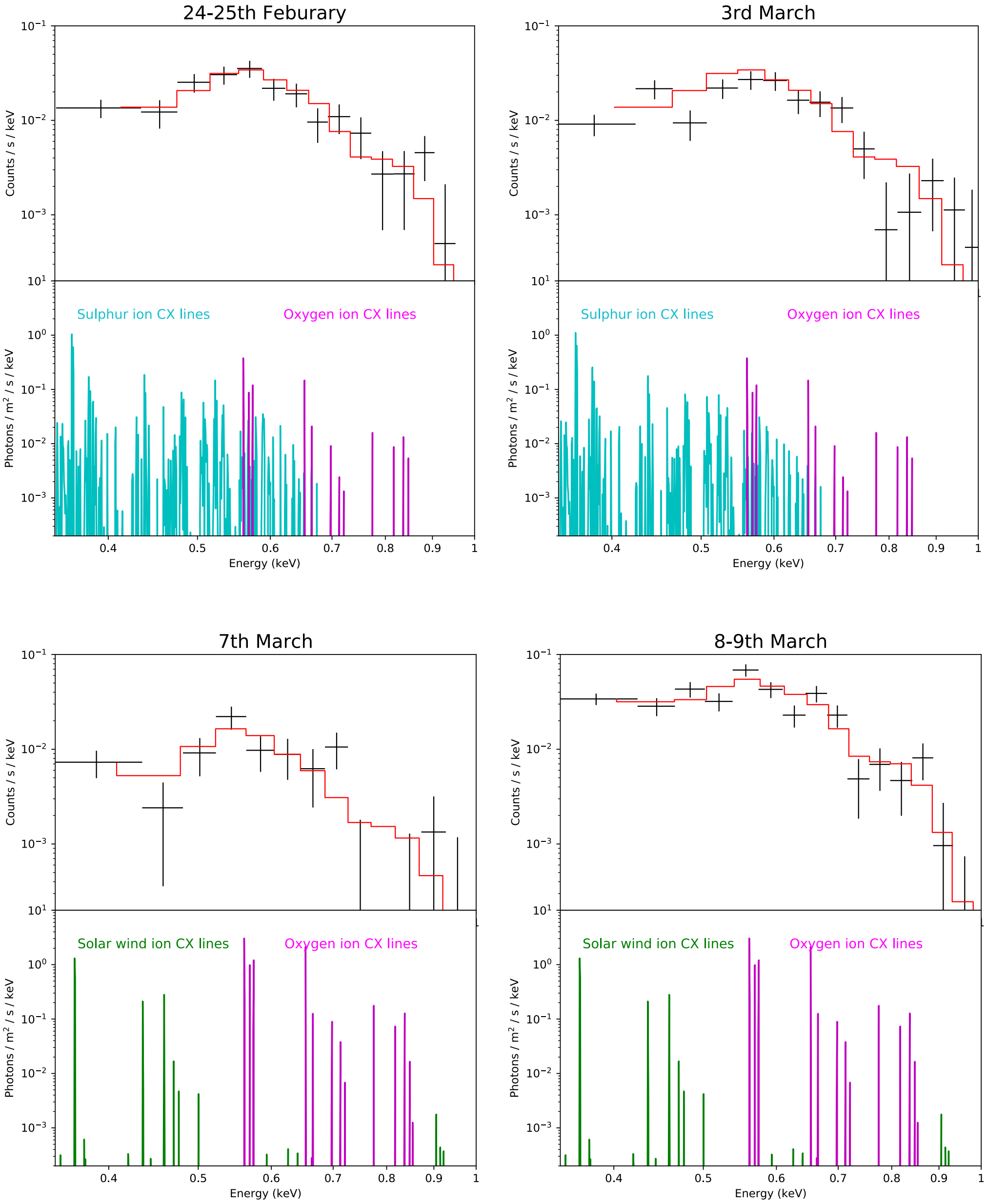

Figure 3.1: Jupiter's auroral spectra fitted by the atomic charge exchange model. The upper panels show the data (black), which were analysed in SPEX. The data are binned by the obin command and fitted with the CX model (red). The lower panels show the best fit theoretical CX line models.

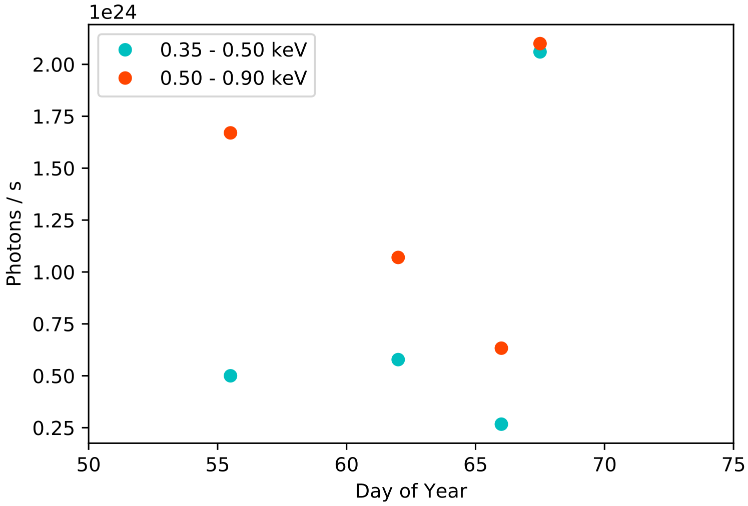

Figure 3.2: Time dependency of number of photons per second from different energy bands of Jupiter's X-ray auroral spectra.

back outwards (CIR day 4 or rarefaction). The magnetospheric expansion hits at 8-9th March, at the time the magnetopause was expanding back to 100 R_J (Dunn et al., 2020b).

In Figure 3.2 we show the time dependency of Jupiter's auroral photon flux. The number of photons per second were determined for different energy bands respectively, as we wanted to determine separately the development of oxygen ion lines contributing from 0.5 - 0.9 keV and sulphur/solar wind ions, which can be found in the 0.35 - 0.5 keV interval. The solar wind velocity, density and dynamic pressure during the time of our observations are shown in Figure 3.3.

The increased solar wind density in Figure 3.3 stands for arrived forward shock on Jupiter's position, corresponding with the peak of solar wind velocity and decreased dynamic pressure. Forward shocks arrived at Jupiter on 23th February and 4th March. Three days after CIR arrival solar wind conditions were turning back to normal and Jupiter's magnetosphere was expected to start expanding (Dunn et al., 2020b).

The photon frequency in the 0.50 - 0.90 keV energy interval decreased during the first three observations. For the 0.35 - 0.50 keV energy band, time dependency of number of photons emitted per second slightly increased between 24-25th February and 3rd March. The lowest flux was observed on 7th March and on 8-9th March, the flux in both energy bands rapidly increased. Figure 3.3 shows no apparent connection between solar wind properties and the photon rates determined. The highest value of solar wind velocity was measured during the 7th March observation, in spite of high solar wind velocity this observation is the dimmest with lowest photon frequency, implying no impact of solar wind velocity on the number of photons. Solar wind density also does not show any correlation with the X-ray observations. 24-25th February measurements took place during the time of high density, despite this fact the photon rate is not higher than during the 8-9th March observation. The peak in density during the 24-25th February observation could reveal connections between the bremsstrahlung continuum emission and the solar wind density since the 24-25th February observation provides the only spectrum that requires the bremsstrahlung emission model.

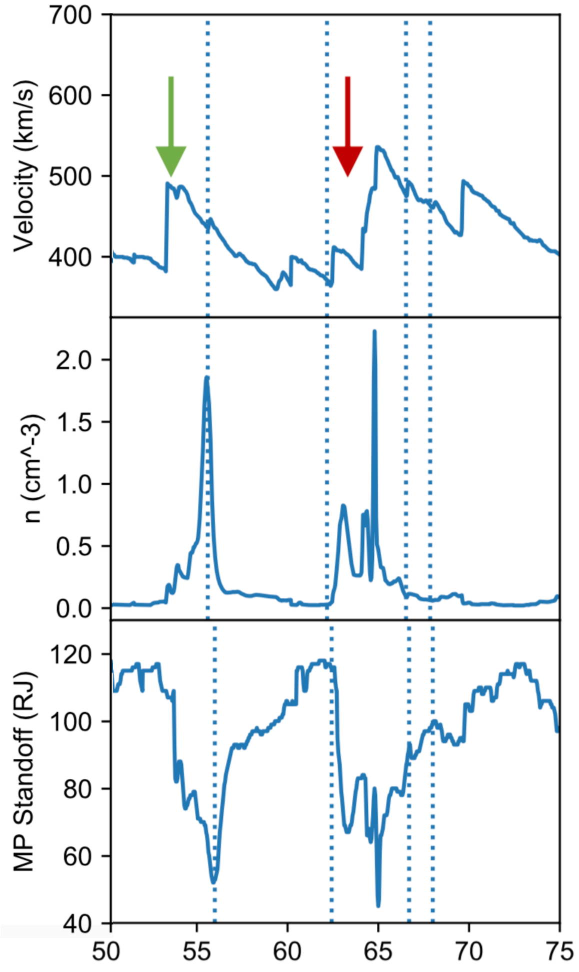

Figure 3.3: Time dependency of solar wind velocity, density and dynamic pressure from Dunn et al. (2020b). The blue dotted lines show the days of observations.

Chapter 4

Discussion

We re-examined four spectra of Jupiter's aurora, observed during the 2007 multi-waveband campaign, including XMM-Newton, Chandra X-ray Observatory, Nançay Decameter Array, WIND spacecraft, Hubble Space Telescope and New Horizons spacecraft measurements. The spectral analysis was carried out by using the SPEX package. Answers to the following questions will be discussed in this chapter. Where is the origin of precipitating ion population? What processes drive the X-ray aurora? To what extent is the solar wind responsible for the X-ray aurora and how are different wavebands linked to each other?

4.1 Origin of X-ray auroral emissions

Our spectral analysis indicates that the solar wind CX model better describes the spectra obtained on 3rd and 8-9th March and the Iogenic CX model better describes the origin of the spectra obtained on 24-25th February and 7th March. Spectra fitted with the same model show similar morphology despite different intensity of their emissions.

Dunn et al. (2020b) provided similar analysis of the data from the campaign in 2007, using the XSPEC spectral fitting package. In their paper Iogenic CX model provided better fit for 24-25th February and 7th March spectra, 8-9th observation showed better fit for solar wind ion model and 3rd March spectrum provided good fit for both models. These results are very similar to ours with comparable final best fit model for each spectra and S:O ratios listed in Table 3.2. Analogous table can be found in Dunn et al. (2020b)in Chapter 6, Table 2. These data mostly corresponds with values determined by us in Chapter 3, exception is measurement on March 7th, when both S:O ratio and ionization temperature diverge. The data obtained during these observations provide large error values, which we expected considering the spectrum quality at this time, when the source was very faint with a small number of counts.

Elsner et al. (2005) performed X-ray spectral analysis of observations carried out by the Chandra ACIS-S instrument over 24–26 February 2003. They suggested magnetospheric origin of Jupiter's aurorae over solar wind origin, based on the connection with other wavebands in correlation with UV flares and X-ray auroral intensity, but the solar wind model could not be fully excluded. The origin was estimated to lie in the outer magnetosphere or the last boundary layer.

The study of X-ray emissions from XMM-Newton measurements of Jupiter in November 2003 was performed by Branduardi-Raymont et al. (2007). They came to the conclusion that the X-ray emission from Jupiter's aurora is well described by the superposition of bremsstrahlung continuum and precipitating CX ions. Similarly with our Gaussian analysis, they found an additional line at 0.83 keV from higher orders of OVIII contaminated with FeXVII emission and MgX line at 1.35 keV. They suggest these lines are reflections of disk emission, as these lines amplified with brightening of the disk.

Dunn et al. (2016) proved interplanetary coronal mass ejection (ICME) influence on X-ray aurorae from two Chandra X-ray observations in October 2011. With the arrival of strong ICME, X-ray spectra seems to be similar to cometary X-ray emissions. Changes in spectral morphology and periodicity were enhanced by this ICME.

Spectral analysis of multi-wavelength observations by the Hisaki satellite, XMM-Newton, and Chandra X-ray Observatory in April 2014 was provided by Kimura et al. (2016). In this paper positive correlation between X-ray auroral core pulsations and solar wind velocity was found, and the position of the auroral core was mapped out to the boundary of the magnetosphere. They suggested a mixture of solar wind ions and magnetospheric ions, mixed up by Kelvin-Helmholtz instabilities.

4.2 Connections between different wavebands

Part of the campaign in 2007 were several UV and radio measurements, which could provide a view of the multi-waveband connections. The UV waveband area can be split into a main oval, a polar aurora region and the moon footprints (Nichols et al., 2009). In the case of a relation between the UV and X-ray aurora, the polar aurora region and the main oval emission seems to exhibit connections with X-rays.

Two forward shocks occurred during our observations. In the case of the solar wind velocity and dynamic pressure increase, brightening of the main oval emission followed. The main auroral oval intensity increased sharply during 23th February. On 6th March there were no measurements in the UV band within two days and after that the main auroral emission was not remarkable. The CIR arrival could change the conditions within the magnetosphere and internal magnetospheric processes could start, initiating the increase of the UV auroral emission intensity (Clarke et al., 2009).

UV emissions could be related to X-rays through quasi-periodic (QP) pulsations. Several hour X-ray observations exhibits 10 seconds to minute pulses in 30% of observations and QP flaring in UV main emission and in the polar region is observed in UV observations with few to 10 minutes periodicity (Dunn et al., 2020b). Kimura et al. (2016) suggested the same source location of this QP UV and X-ray aurora pulsations.

Branduardi-Raymont et al. (2008) studied the connections between the bremsstrahlung X-rays and FUV emissions, suggesting the same population of energetic electrons may be responsible for both hard X-ray and FUV emissions from Jupiter's auroral regions as FUV emission originates from energetic electrons interacting with H and H_2 molecules in excited states and decelerated electrons are responsible for hard X-ray emission. Since the February 24-25th spectrum was only one with relevant bremsstrahlung X-ray emission and the auroral brightening occurred one day before the start of the observation, the FUV emission could be connected with our X-ray observation during this date. Dunn et al. (2020b) suggested only UV main emission with power greater than 1 TW is significant for hard X-ray emission. The UV power was greater than 1 TW only during the 24-25th February observation and for the rest UV power was $\sim$ 500 GW and the bremsstrahlung emission was absent.

In the radio band bursts of decametric emission (DAM) take place. These bursts need to be filtered to discard bursts originating from Io-Jupiter interaction. Non-Io DAM bursts should be triggered by solar wind compression and rarefaction. Radio observations by Dunn et al. (2020b) indeed show a connection between radio DAM bursts and solar wind driven compression with following expansion. They show that very bright non-Io DAM bursts occurred at 10th March after the brightest UV emission of the campaign, which would mean relation of non-Io DAM bursts and powerful UV aurora. Relation between radio and X-ray observations is again in the QP pulsation as in the case of UV measurements. Similarly pulses appeared during radio analysis with similar periodicity as in X-ray analysis. These pulses seems to occur during the time of X-ray aurora brightening.

A closer look at infrared auroral emission was made by Stallard et al. (2016), where they studied infrared images taken between 1995 and 2000. The H_3^+ molecule is responsible for this aurora. The pulses with periodicity of $\sim$ 30 minutes were found but no time variation lower than 30 minutes appeared. Watanabe et al. (2018) also performed a study of Jupiter's IR auroral emission for observations taken on 25 May 2016. In their paper, periodicity of $\sim$ 10 minutes was determined, but no UV measurements were taken at this date so correlation with the UV aurora could not be resolved. This periodicity could be possibly connected with pulses in other wavebands

4.3 Comparison with X-rays from other planets in the Solar system

Earth

On Earth auroral, non-auroral and geocoronal X-ray emission are observable. Precipitating particles inside Earth's magnetosphere react with the upper at-

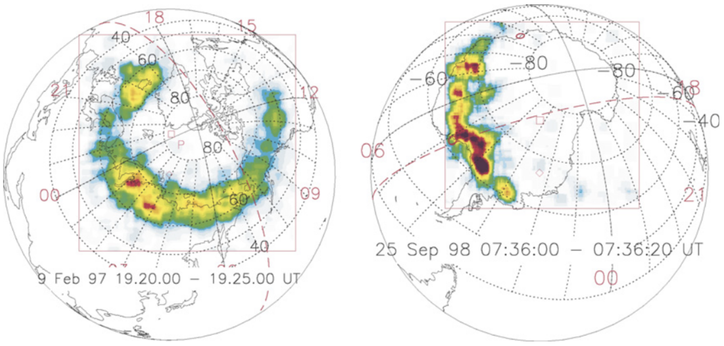

Figure 4.1: X-ray auroral image of Earth taken by the Polar PIXIE instrument (Bhardwaj et al., 2007).

mosphere, creating aurora, emitting visible, UV and X-ray light. This process gives rise to characteristic emission lines in X-ray spectra, typically Nitrogen, Oxygen and Argon. Spectral lines are caused by precipitating particles reacting with electrons from the atmospheric atoms. Accelerated electrons also produce continuous bremsstrahlung emission. Compared to Jupiter's auroral emission, where soft X-rays are caused by highly charged ions undergoing charge exchange with atmospheric neutrals, Earth's aurora is created due to fast precipitating particles, e.g. electrons or protons. Non-auroral emission is negligible above 2 keV, on the other hand soft X-rays were observed even during quite Sun conditions. Two causes can be responsible for soft non-auroral X-rays, Thompson scattering from electrons in atoms and molecules inside atmosphere and absorption of incident solar X-rays followed by characteristic line emission. The geocoronal X-ray emission shows sign of charge exchange. This emission is dependant on solar wind condition and with increased solar wind flux, the distance of the magnetopause decreases and solar wind ions can get to places with higher densities, which increase the X-ray intensities (Bhardwaj et al., 2007). The Solar wind Magnetosphere Ionosphere Link Explorer (SMILE) spacecraft is planned to launch in November 2023. SMILE will image Earth's magnetosphere in soft X-ray and UV band and it will provide better view on interaction between the solar wind and Earth's magnetosphere.

Venus and Mars

Unlike Jupiter, Saturn or Earth, Venus lacks magnetic field and therefore there is no auroral emission. Solar wind thus reacts directly with Venus's ionosphere. Venus has the highest optical surface after the Sun and because X-ray telescopes with CCDs are sensitive to optical light, it is hard to observe it in the X-ray band. The X-ray appearance of Venus consists of disk emission caused by fluorescent scattering of solar X-rays. There also exists a possibility for charge exchange happening in the outer atmosphere, but unfortunately observations are not

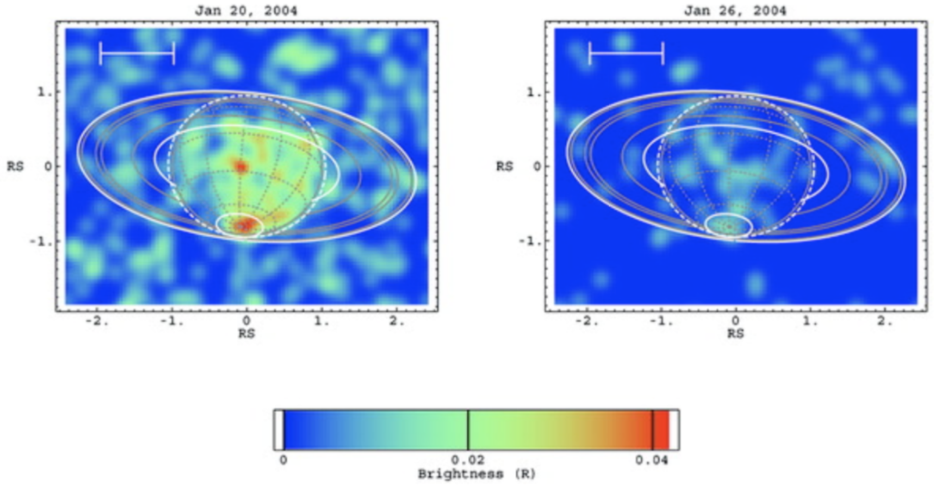

Figure 4.2: X-ray images of Saturn taken by Chandra one week apart in January 2004. From Badman et al. (2015).

sensitive enough to detect such emission (Dennerl, K. et al., 2002).

Mars has a small and weak magnetosphere and therefore its X-ray appearance differs from Jupiter's. Similarly to Venus there are no signs of polar X-ray emission. Martian X-ray observations show high count rate from the disk of the size of the planet. These X-rays are caused by fluorescent scattering of solar X-rays, same as in the case of Venus. Bremsstrahlung emission also contributes to the X-ray emission. An X-ray halo surrounding the planet has also been detected with a lower count rate. Solar wind charge exchange can well explain the emission from the halo (Gunell et al., 2004).

Saturn

Saturn's magnetosphere shows similar complexity to Jupiter's. Analogously in the case of the moons, Titan and Enceladus are orbiting Saturn. Therefore the same processes that are present on Jupiter are expected to be found on Saturn, which include X-ray auroral emission in the polar region caused by solar wind charge exchange. Yet this emission was not found in Saturn's X-rays. Both disk and auroral X-ray emission are dependant on the solar wind conditions, which indicates that Saturn's polar X-ray emission is just extended emission from disk region, for which scattering of solar X-rays is probably responsible. X-ray emission from Saturn's rings was also revealed with the dominance of a single oxygen line. That possibly results from excitation of oxygen trapped in ice water particles inside the ring. This oxygen line, however, shows a lack of correlation with solar wind conditions and it was suggested that oxygen is excited by electron injections from the planet's thunderstorms (Bhardwaj et al., 2007) (Badman et al., 2015).

Chapter 5

Summary and Conclusion

We presented a spectral analysis of four Jupiter's auroral spectra obtained between 24-25th February and 8-9th March. We fitted the observed spectra with a CX model using the SPEX spectral fitting package in order to determine the processes that are responsible for the auroral X-ray emission of Jupiter.

We find two X-ray emission mechanisms in Jupiter's auroare, bremsstrahlung and charge exchange. The CX process occurs, when highly charged "projectile" ions collide with "target" neutral atoms in the atmosphere. During the collision the neutral atom exchanges an electron with the ion, and the electron then decays and emits an X-ray photon. The question is whether the projectile ions originate in the Jovian magnetosphere or in the solar wind. Due to surface sublimation and volcanic activity, the galilean moon Io leaks particles from its SO_2 atmosphere, creating a plasma sheet inside Jupiter's magnetosphere. Nevertheless highly charged ions (mainly carbon and oxygen ions) in the solar wind plasma can also get inside Jupiter's magnetosphere. Both types of plasma particles could then be captured by field-aligned current systems, where they would be accelerated and consequently would precipitate in Jupiter's atmosphere, where they undergo CX, creating X-ray auroral emission.

Our goal was to determine the origin of the highly charged ions. We fitted the spectra with S:O model, which would indicate Io origin and with a solar wind charge exchange model suggesting solar wind origin. The spectrum observed on 24-25th February was better fitted by the S:O model and the spectrum observed on 8-9th March was better described by the solar wind model. The spectra from 3rd and 7th March could be fit by both models. These results indicates that both models could be responsible for Jupiter's X-ray auroral emission. We determined the photon flux for every observation and we compared it with the solar wind conditions during our measurements from Dunn et al. (2020b). We find that neither the photon flux nor the spectral properties show connection with the solar wind conditions. Therefore, despite the fact that our fits were similarly good for both models, no connection with solar wind conditions supports the S:O iogenic origin. We also added a bremsstrahlung emission model to our fits and this model provided a better fit only for the spectrum obtained on 24-25th February. Because at this time, the solar wind density was higher, we conclude that X-ray bremsstrahlung emission is connected with the solar wind.

There remains the possibility that both plasma species interacts at the magnetopause region and a mix of solar wind ions and ions from the plasma sheet create the X-ray aurora. The problem with this model is that solar wind ions have different energy than ions from the plasma sheet and they would have to undergo different potential drops in order to gain energy, which was detected.

Bibliography

Sarah V. Badman, Graziella Branduardi-Raymont, Marina Galand , Sébastien L. G. Hess, Norbert Krupp, Laurent Lamy, Henrik Melin, and Chihiro Tao. Auroral Processes at the Giant Planets: Energy Deposition, Emission Mechanisms, Morphology and Spectra. Space Sci. Rev., 187(1-4):99–179, April 2015. doi: 10.1007/s11214-014-0042-x.

F. Bagenal, A. Adriani, F. Allegrini, S. J. Bolton, B. Bonfond, E. J. Bunce, J. E. P. Connerney, S. W. H. Cowley, R. W. Ebert, G. R. Gladstone, C. J. Hansen, W. S. Kurth, S. M. Levin, B. H. Mauk, D. J. McComas, C. P. Paranicas, D. Santos-Costa, R. M. Thorne, P. Valek, J. H. Waite, and P. Zarka. Magnetospheric Science Objectives of the Juno Mission. Space Sci. Rev., 213 (1-4):219–287, November 2017. doi: 10.1007/s11214-014-0036-8.

Anil Bhardwaj, Ronald F. Elsner, G. Randall Gladstone, Thomas E. Cravens, Carey M. Lisse, Konrad Dennerl, Graziella Branduardi-Raymont, Bradford J. Wargelin, J. Hunter Waite, Ina Robertson, Nikolai Østgaard, Peter Beiersdorfer, Steven L. Snowden, and Vasili Kharchenko. X-rays from solar system objects. *Planetary and Space Science*, 55(9):1135 – 1189, 2007. ISSN 0032-0633. doi: https://doi.org/10.1016/j.pss.2006.11.009. Highlights in Planetary Science.

G. Branduardi-Raymont, A. Bhardwaj, R. F. Elsner, G. R. Gladstone, G. Ramsay, P. Rodriguez, R. Soria, Jr. Waite, J. H., and T. E. Cravens. A study of Jupiter's aurorae with XMM-Newton. A&A, 463(2):761–774, February 2007. doi: 10.1051/0004-6361:20066406.

G. Branduardi-Raymont, R. F. Elsner, M. Galand, D. Grodent, T. E. Cravens, P. Ford, G. R. Gladstone, and J. H. Waite. Spectral morphology of the X-ray emission from Jupiter's aurorae. *Journal of Geophysical Research (Space Physics)*, 113(A2):A02202, February 2008. doi: 10.1029/2007JA012600.

J. T. Clarke, D. Grodent, S. W. H. Cowley, E. J. Bunce, P. Zarka, J. E. P. Connerney, and T. Satoh. *Jupiter's Aurora*, page 639. 2007.

J. T. Clarke, J. Nichols, J. C. Gérard, D. Grodent, K. C. Hansen, W. Kurth, G. R. Gladstone, J. Duval, S. Wannawichian, E. Bunce, S. W. H. Cowley, F. Crary, M. Dougherty, L. Lamy, D. Mitchell, W. Pryor, K. Retherford,

T. Stallard, B. Zieger, P. Zarka, and B. Cecconi. Response of Jupiter's and Saturn's auroral activity to the solar wind. *Journal of Geophysical Research (Space Physics)*, 114(A5):A05210, May 2009. doi: 10.1029/2008JA013694.

John T. Clarke. Auroral Processes on Jupiter and Saturn. *Washington DC American Geophysical Union Geophysical Monograph Series*, 197:113–121, January 2012. doi: 10.1029/2011GM001199.

S. W. H. Cowley and E. J. Bunce. Origin of the main auroral oval in Jupiter's coupled magnetosphere-ionosphere system. Planet. Space Sci., 49(10-11): 1067–1088, August 2001. doi: 10.1016/S0032-0633(00)00167-7.

T. E. Cravens. Comet Hyakutake x-ray source: Charge transfer of solar wind heavy ions. Geophys. Res. Lett., 24(1):105–108, January 1997. doi: 10.1029/96GL03780.

T. E. Cravens, J. H. Waite, T. I. Gombosi, N. Lugaz, G. R. Gladstone, B. H. Mauk, and R. J. MacDowall. Implications of Jovian X-ray emission for magnetosphere-ionosphere coupling. *Journal of Geophysical Research (Space Physics)*, 108(A12):1465, December 2003. doi: 10.1029/2003JA010050.

Thomas E. Cravens. Heliospheric x-ray emission associated with charge transfer of the solar wind with interstellar neutrals. *The Astrophysical Journal*, 532(2): L153–L156, apr 2000. doi: 10.1086/312574.

J. W. den Herder, Brinkman, A. C., Kahn, S. M., Branduardi-Raymont, G., Thomsen, K., Aarts, H., Audard, M., Bixler, J. V., den Boggende, A. J., Cottam, J., Decker, T., Dubbeldam, L., Erd, C., Goulooze, H., Güdel, M., Guttridge, P., Hailey, C. J., Al Janabi, K., Kaastra, J. S., de Korte, P. A. J., van Leeuwen, B. J., Mauche, C., McCalden, A. J., Mewe, R., Naber, A., Paerels, F. B., Peterson, J. R., Rasmussen, A. P., Rees, K., Sakelliou, I., Sako, M., Spodek, J., Stern, M., Tamura, T., Tandy, J., de Vries, C. P., Welch, S., and Zehnder, A. The reflection grating spectrometer on board xmm-newton. *A&A*, 365(1):L7–L17, 2001. doi: 10.1051/0004-6361:20000058.

Dennerl, K., Burwitz, V., Englhauser, J., Lisse, C., and Wolk, S. Discovery of x-rays from venus with chandra. *A&A*, 386(1):319–330, 2002. doi: 10.1051/0004-6361:20020097.

W. R. Dunn, G. Branduardi-Raymont, V. Carter-Cortez, A. Campbell, R. Elsner, J-U. Ness, G. R. Gladstone, P. Ford, Z. Yao, P. Rodriguez, G. Clark, C. Paranicas, A. Foster, R. Gray, S. V. Badman, L. C. Ray, E. J. Bunce, B. Snios, C. M. Jackman, I. J. Rae, R. Kraft, A. Rymer, S. Lathia, and N. Achilleos. Jupiter's X-rays 2007 Part 1: Jupiter's X-ray Emission During Solar Minimum. in preparation, 2020a.

W. R. Dunn, R. Grey, A. D. Wibisono, S. V. Badman, G. Branduardi-Raymont, R. Elsner, G. R. Gladstone, R. Ebert, L. Lamy, C. Louis, P. Ford, A. Foster,

C. Tao, L. C. Ray, Z. Yao, I. J. Rae, E. J. Bunce, P. Rodriguez, C. M. Jackman, G. Nicolaou, J. Clarke, J. Nichols, H. Elliott, and R. Kraft. Jupiter's X-ray Emission 2007 Part 2: Comparisons with UV and Radio Emissions and In-Situ Solar Wind Measurements. in preparation, 2020b.

William R. Dunn, Graziella Branduardi-Raymont, Ronald F. Elsner, Marissa F. Vogt, Laurent Lamy, Peter G. Ford, Andrew J. Coates, G. Randall Gladstone, Caitriona M. Jackman, Jonathan D. Nichols, I. Jonathan Rae, Ali Varsani, Tomoki Kimura, Kenneth C. Hansen, and Jamie M. Jasinski. The impact of an ICME on the Jovian X-ray aurora. *Journal of Geophysical Research (Space Physics)*, 121(3):2274–2307, March 2016. doi: 10.1002/2015JA021888.

R. F. Elsner, N. Lugaz, J. H. Waite, T. E. Cravens, G. R. Gladstone, P. Ford, D. Grodent, A. Bhardwaj, R. J. MacDowall, M. D. Desch, and T. Majeed. Simultaneous Chandra X ray, Hubble Space Telescope ultraviolet, and Ulysses radio observations of Jupiter's aurora. *Journal of Geophysical Research (Space Physics)*, 110(A1):A01207, January 2005. doi: 10.1029/2004JA010717.

Liyi Gu, Jelle Kaastra, and A. J. J. Raassen. Plasma code for astrophysical charge exchange emission at X-ray wavelengths. A&A, 588:A52, April 2016. doi: 10.1051/0004-6361/201527615.

H. Gunell, M. Holmström, E. Kallio, P. Janhunen, and K. Dennerl. X rays from solar wind charge exchange at mars: A comparison of simulations and observations. *Geophysical Research Letters*, 31(22), 2004. doi: 10.1029/2004GL020953.

T. W. Hill. The Jovian auroral oval. J. Geophys. Res., 106(A5):8101–8108, May 2001. doi: 10.1029/2000JA000302.

F. Jansen, Lumb, D., Altieri, B., Clavel, J., Ehle, M., Erd, C., Gabriel, C., Guainazzi, M., Gondoin, P., Much, R., Munoz, R., Santos, M., Schartel, N., Texier, D., and Vacanti, G. Xmm-newton observatory* - i. the spacecraft and operations. *A&A*, 365(1):L1–L6, 2001. doi: 10.1051/0004-6361:20000036.

J. S. Kaastra, R. Mewe, and H. Nieuwenhuijzen. SPEX: a new code for spectral analysis of X & UV spectra. In *UV and X-ray Spectroscopy of Astrophysical and Laboratory Plasmas*, pages 411–414, January 1996.

Krishan K. Khurana, Margaret G. Kivelson, Vytenis M. Vasyliunas, Norbert Krupp, Joachim Woch, Andreas Lagg, Barry H. Mauk, and William S. Kurth. *The configuration of Jupiter's magnetosphere*, chapter 24. Cambridge University Press, 2004. ISBN 0-521-81808-7.

T. Kimura, R. P. Kraft, R. F. Elsner, G. Brand uardi-Raymont, G. R. Gladstone, C. Tao, K. Yoshioka, G. Murakami, A. Yamazaki, F. Tsuchiya, M. F. Vogt, A. Masters, H. Hasegawa, S. V. Badman, E. Roediger, Y. Ezoe, W. R. Dunn, I. Yoshikawa, M. Fujimoto, and S. S. Murray. Jupiter's X-ray and EUV auroras monitored by Chandra, XMM-Newton, and Hisaki satellite. *Journal of Geophysical Research (Space Physics)*, 121(3):2308–2320, March 2016. doi: 10.1002/2015JA021893.

C. M. Lisse, K. Dennerl, J. Englhauser, M. Harden, F. E. Marshall, M. J. Mumma, R. Petre, J. P. Pye, M. J. Ricketts, J. Schmitt, J. Trumper, and R. G. West. Discovery of X-ray and Extreme Ultraviolet Emission from Comet C/Hyakutake 1996 B2. *Science*, 274(5285):205–209, October 1996. doi: 10.1126/science.274.5285.205.

Barry H. Mauk and Joachim Saur. Equatorial electron beams and auroral structuring at Jupiter. *Journal of Geophysical Research (Space Physics)*, 112 (A10):A10221, October 2007. doi: 10.1029/2007JA012370.

J. D. Nichols, J. T. Clarke, J. C. Gérard, D. Grodent, and K. C. Hansen. Variation of different components of Jupiter's auroral emission. *Journal of Geophysical Research (Space Physics)*, 114(A6):A06210, June 2009. doi: 10.1029/2009JA014051.

Tom S. Stallard, John T. Clarke, Henrik Melin, Steve Miller, Jon D. Nichols, James O'Donoghue, Rosie E. Johnson, John E. P. Connerney, Takehiko Satoh, and Michael Perry. Stability within Jupiter's polar auroral 'Swirl region' over moderate timescales. Icarus, 268:145–155, April 2016. doi: 10.1016/j.icarus.2015.12.044.

L. Strüder, Briel, U., Dennerl, K., Hartmann, R., Kendziorra, E., Meidinger, N., Pfeffermann, E., Reppin, C., Aschenbach, B., Bornemann, W., Bräuninger, H., Burkert, W., Elender, M., Freyberg, M., Haberl, F., Hartner, G., Heuschmann, F., Hippmann, H., Kastelic, E., Kemmer, S., Kettenring, G., Kink, W., Krause, N., Müller, S., Oppitz, A., Pietsch, W., Popp, M., Predehl, P., Read, A., Stephan, K. H., Stötter, D., Trümper, J., Holl, P., Kemmer, J., Soltau, H., Stötter, R., Weber, U., Weichert, U., von Zanthier, C., Carathanassis, D., Lutz, G., Richter, R. H., Solc, P., Böttcher, H., Kuster, M., Staubert, R., Abbey, A., Holland, A., Turner, M., Balasini, M., Bignami, G. F., La Palombara, N., Villa, G., Buttler, W., Gianini, F., Lainé, R., Lumb, D., and Dhez, P. The european photon imaging camera on xmm-newton: The pn-ccd camera *. *A&A*, 365(1):L18–L26, 2001. doi: 10.1051/0004-6361:20000066.

Turner, L., Abbey, A., Arnaud, M., Balasini, M., Barbera, M., Belsole, E., Bennie, P. J., Bernard, J. P., Bignami, G. F., Boer, M., Briel, U., Butler, I., Cara, C., Chabaud, C., Cole, R., Collura, A., Conte, M., Cros, A., Denby, M., Dhez, P., Di Coco, G., Dowson, J., Ferrando, P., Ghizzardi, S., Gianotti, F., Goodall, C. V., Gretton, L., Griffiths, R. G., Hainaut, O., Hochedez, J. F., Holland, A. D., Jourdain, E., Kendziorra, E., Lagostina, A., Laine, R., La Palombara, N., Lortholary, M., Lumb, D., Marty, P., Molendi, S., Pigot, C., Poindron, E., Pounds, K. A., Reeves, J. N., Reppin, C., Rothenflug, R., Salvetat, P., Sauvageot, J. L., Schmitt, D., Sembay, S., Short, A. D. T., Spragg, J., Stephen, J., Strüder, L., Tiengo, A., Trifoglio, M., Trümper, J., Vercellone, S., Vigroux, L., Villa, G., Ward, M. J., Whitehead, S., and Zonca, E. The european photon imaging camera on xmm-newton: The mos cameras. *A&A*, 365(1):L27–L35, 2001. doi: 10.1051/0004-6361:20000087.

R. von Steiger, N. A. Schwadron, L. A. Fisk, J. Geiss, G. Gloeckler, S. Hefti, B. Wilken, R. F. Wimmer-Schweingruber, and T. H. Zurbuchen. Composition of quasi-stationary solar wind flows from Ulysses/Solar Wind Ion Composition Spectrometer. J. Geophys. Res., 105(A12):27217–27238, December 2000. doi: 10.1029/1999JA000358.

B. J. Wargelin, P. Beiersdorfer, and G. V. Brown. EBIT charge-exchange measurements and astrophysical applications. *Canadian Journal of Physics*, 86(1):151–169, January 2008. doi: 10.1139/P07-125.

Bradford J. Wargelin and Jeremy J. Drake. Observability of stellar winds from late-type dwarfs via charge exchange x-ray emission. *The Astrophysical Journal*, 546(1):L57–L60, jan 2001. doi: 10.1086/318066.

H. Watanabe, H. Kita, C. Tao, M. Kagitani, T. Sakanoi, and Y. Kasaba. Pulsation Characteristics of Jovian Infrared Northern Aurora Observed by the Subaru IRCS with Adaptive Optics. Geophys. Res. Lett., 45(21):11,547–11,554, November 2018. doi: 10.1029/2018GL079411.